Chapter 2
Fundamentals of Metamaterial Structures

2.1 Introduction to Metamaterials

In the last decade a new research area based on the study of Metamaterials has emerged. There is not an absolute definition of Metamaterials but the most commonly used is that they are artificial materials made of a periodic arrangement of unit cells much smaller than the wavelength with some unique properties [1–3]. Such properties include a simultaneous negative permittivity and permeability that translates into a negative refractive index, these structures are commonly referred as left-handed materials (LHM). By using LHM in the design of a structure, its properties can be tailored in a broader manner than with classical materials. Interesting effects can be observed in the propagation of the electromagnetic waves, for example, backward propagation of waves due to an antiparallel group and phase velocity resulting in the backward travel of the wavefronts while the energy still travels forward away from the source to satisfy causality. Another desired effect is the significant reduction in size compared to classical structures that can be achieved for certain conditions relevant to a specific design. Metamaterials can be used for several interesting devices in microwave and terahertz engineering such as antennas, sensors, matching networks or new superlens with a higher focusing capability than conventional ones in areas such as telecommunications and biomedical applications.

The concept of LHM was first developed by a Russian physicist Victor Veselago in 1967 [4]. He predicted the existence of materials that could allow the propagation of electromagnetic waves with an electric field, magnetic field and phase vector that form a left-handed triad opposite to the commonly known right-handed triad of conventional materials (RHM). He also demonstrated that such materials are allowed by the Maxwell's equations. The most important electromagnetic properties discovered by Veselago are the reversal of Snell's Law, the reversal of the Doppler effect and the reversal of Vavilov-Cerenkov radiation. The cuspid of his work is not represented by the use of LHM in 1-dimensional structures but furthermore

M. Puentes Vargas, *Planar Metamaterial Based Microwave Sensor Arrays for Biomedical Analysis and Treatment*, Springer Theses,
DOI: 10.1007/978-3-319-06041-5_2, © Springer International Publishing Switzerland 2014

in the realization of 2-dimensional and 3-dimensional isotropic and homogeneous media that can support backward waves and have a negative refractive index. Further analysis on his work can be found in [5] and [6].

Since Metamaterials are artificial materials and some of its properties are not found in nature, it is important that the Maxwell's equations are satisfied to obtain a physical meaningful result. The Maxwell's equations in its differential form are given as follows

$$\nabla \times \bar{E} = \frac{-\partial \bar{B}}{\partial t} - \bar{M} \tag{2.1}$$

$$\nabla \times \bar{H} = \frac{-\partial \bar{D}}{\partial t} + \bar{J} \tag{2.2}$$

$$\nabla \times \bar{D} = \rho \tag{2.3}$$

$$\nabla \times \bar{B} = 0 \tag{2.4}$$

where $\bar{E}(V/m)$ is the electric field density, $\bar{H}(A/m)$ is the magnetic field density, $\bar{D}(C/m^2)$ is the electric flux density, $\bar{B}(W/m^2)$ is the magnetic flux density, $\bar{M}(V/m^2)$ is the (fictitious) magnetic current density, $\bar{J}(A/m^2)$ is the electric current density and $\rho(C/m^3)$ is the electric charge density. If the medium is linear, non-dispersive, homogeneous and isotropic additional constitutive relations are given as follows

$$\bar{D} = \varepsilon_0 \bar{E} + \bar{P} = \varepsilon_0(1 + \chi_e)\bar{E} = \varepsilon_0 \varepsilon_r \bar{E} = \varepsilon \bar{E} \tag{2.5}$$

$$\varepsilon_r = \varepsilon' - j\varepsilon'' \tag{2.6}$$

$$\bar{B} = \mu_0(\bar{H} + \bar{M}) = \mu_0(1 + \chi_m)\bar{H} = \mu_0 \mu_r \bar{H} = \mu \bar{H} \tag{2.7}$$

$$\mu_r = \mu' - j\mu'' \tag{2.8}$$

where $\bar{P}$ and $\bar{M}$ are the electric and magnetic polarization, χ_e and χ_m are the electric and magnetic susceptibility, ε_0 and μ_0 are the permittivity and permeability of free space and ε_r and μ_r are the permittivity and permeability of the material in question.

By considering a harmonic time-dependent plane wave traveling in the x-direction with electric field polarized in z-direction in a homogeneous, isotropic and linear medium, the Helmholtz wave equation looks as follows [7]

$$\frac{\partial^2}{\partial x^2} E_z(x) + \omega^2 \mu \varepsilon \, E_z(x) = 0 \tag{2.9}$$

$$\frac{\partial^2}{\partial y^2} H_y(x) + \omega^2 \mu \varepsilon \, H_y(x) = 0. \tag{2.10}$$

Assuming harmonic fields with time dependance $e^{j\omega t}$, the solution of $E_z(x)$ and $H_y(x)$ can be given as

$$E_z(x) = C_1 e^{-j\gamma x} + C_2 e^{j\gamma x} \tag{2.11}$$

$$H_y(x) = \frac{1}{\eta}(C_1 e^{-j\gamma x} + C_2 e^{j\gamma x}), \tag{2.12}$$

with

$$\gamma = \pm j\omega\sqrt{\mu\varepsilon} \tag{2.13}$$

$$\eta = \sqrt{\frac{\mu}{\varepsilon}}, \tag{2.14}$$

where η (Ω) is the wave impedance for the plane wave, defined as the ratio of the $\bar{E}$ and $\bar{H}$ fields and γ ($1/m$) is the propagation constant. Since any physical scenario can be expressed as the superposition of plane waves of different frequencies according to the Fourier transform theorem, by considering a single plane wave the necessary information of the fundamental response of the medium can be obtained.

When considering a lossless medium and assuming that both μ and ε are positive, the propagation constant is purely imaginary and the plane wave will propagate outward from the source. When considering a more general case where μ and ε can take any value, including a simultaneous negative value, the propagation constant behaves in a more complicated fashion and both real and imaginary part of it has to be taken into account and it is given by

$$\gamma = \alpha + j\beta = \pm j\omega\sqrt{\mu\varepsilon}\sqrt{1 - j\frac{\sigma}{\omega\varepsilon}}, \tag{2.15}$$

where σ is the conductivity. Since the interest is on analyzing if LHMs are viable in terms of causality and therefore be used to construct periodic structures, the case of having both μ and ε negative will be addressed. By inserting this consideration into Eq. 2.15, one can notice that the attenuation constant α remains undisturbed as compared to having both variables positive, the interesting change occurs in the phase constant β. The β for RHM is positive and for LHM is negative. This results in a forward (away from the source) travel of the equiphase fronts for the RHM and a backward (towards the source) for the LHM. To satisfy causality in the LHM, it should be carefully analyzed what exactly propagates towards the source. The propagation of energy is not necessarily the same as the propagation of the equiphase fronts, for LHM they have opposite directions, this means, that energy will always propagate forward while the equiphase fronts move backwards. This can be seen in the phase velocity v_p and group velocity v_g as follows

$$v_p = \frac{\omega}{\beta} \tag{2.16}$$

$$v_g = \frac{\partial \omega}{\partial \beta}, \tag{2.17}$$

and the propagation characteristics for both RHM and LHM can be summarized by

$$\text{RHM} : \beta > 0, v_p > 0, v_g > 0 \tag{2.18}$$

$$\text{LHM} : \beta < 0, v_p < 0, v_g > 0. \tag{2.19}$$

Although the idea of a backward propagation seems troubling at first, it takes an interesting meaning once is realized that the phase velocity corresponds only to the propagation of a perturbation and not of energy itself. A negative group velocity would on the other hand be completely unpractical and would violate the law of causality. Since it has been proven that LHM can be fabricated [2] and be used to interact with electromagnetic waves, in the following sections will be addressed two different ways to physically use them and analyze them. The first one is as a transmission line structure and the second is an arrangement of resonant particles. Both approaches are useful for specific applications and are used throughout the work presented here in several different sensing scenarios. For this reason a comprehensible analysis of both approaches will be presented in this chapter.

2.2 Composite Right/Left Handed Transmission Line

Metamaterials are effective homogeneous materials that under certain assumptions can be modeled as a transmission line. They were first introduced in [1] and [3]. To consider them as a homogeneous material the key assumption is that a left-handed unit cell has an incremental length dz and the following restriction has to be applied

$$dz \ll \lambda_g = \frac{2\pi}{\beta}, \tag{2.20}$$

where λ_g represents the guided wavelength. In Fig. 2.1 is shown a section of an ideal transmission line. Inside the series impedance Z' and shunt inductance Y' different arrangement of lumped elements can be included. Two well known are the pure right-handed transmission line (PRH-TL) presented in Fig. 2.2a and the pure left-handed transmission line (PLH-TL) depicted in Fig. 2.2b. As mentioned before the LH-TL has some unique properties that can offer interesting features. Unfortunately in reality it is impossible to construct a PLH-TL since parasitic effects are unavoidable. The result is the composite right-left handed transmission line (CRLH-TL) shown in Fig. 2.2c.

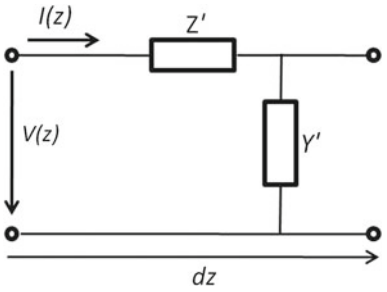

Fig. 2.1 Ideal homogeneous transmission line segment in the form of its incremental model

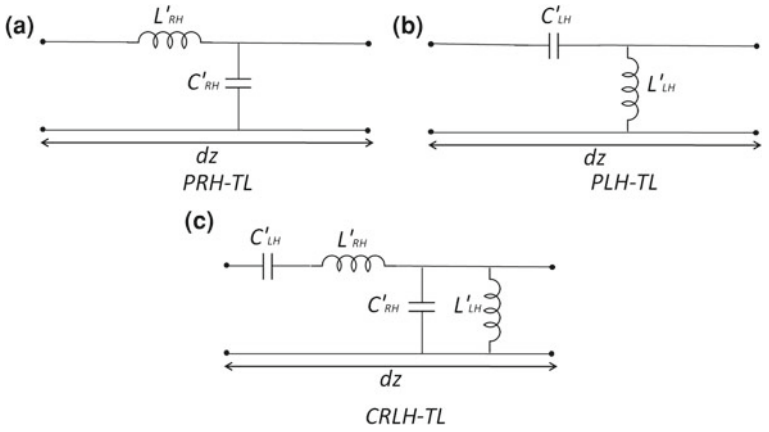

Fig. 2.2 Unit cell configurations: **a** PRH-TL, **b** PLH-TL and **c** CRLH-TL [5]

The propagation constant of any TL and the line impedance is given by [7]

$$\gamma = \alpha + j\beta = \sqrt{Z'Y'} \tag{2.21}$$

$$Z_L = R_L + jX_L = \sqrt{\frac{Z'}{Y'}} \tag{2.22}$$

where Z' and Y' are the per-unit length impedance and admittance respectively. For the CRLH-TL case they look as follows

$$Z' = j\left(\omega L'_{RH} - \frac{1}{\omega C'_{LH}}\right) \tag{2.23}$$

$$Y' = j\left(\omega C'_{RH} - \frac{1}{\omega L'_{LH}}\right). \tag{2.24}$$

By inserting Eqs. 2.23 and 2.24 into Eqs. 2.21 and 2.22 we obtain [8]

$$\gamma^{CRLH} = \pm j\omega\sqrt{\left(L'_{RH} - \frac{1}{\omega^2 C'_{LH}}\right)\left(C'_{RH} - \frac{1}{\omega^2 L'_{LH}}\right)} \tag{2.25}$$

$$Z_L^{CRLH} = \pm\sqrt{\frac{L'_{RH} - \frac{1}{\omega^2 C'_{LH}}}{C'_{RH} - \frac{1}{\omega^2 L'_{LH}}}}, \tag{2.26}$$

where Z_{LH} is the PLH impedance

$$Z_{LH} = \sqrt{\frac{L'_{LH}}{C'_{LH}}} \tag{2.27}$$

and Z_{RH} is the PRH impedance

$$Z_{RH} = \sqrt{\frac{L'_{RH}}{C'_{RH}}}. \tag{2.28}$$

At low frequencies the RH contribution will tend to zero and the line will behave as a PLH-TL, at high frequencies the LH contribution will tend to zero and the line will behave as a PRH-TL. At all other frequencies, the transmission behavior would be a combination of the RH and LH components and will result in a band gap. The limits of the band gap can be obtained with the correspondent series and parallel resonance frequencies f_s and f_p as follows

$$f_s = \frac{\omega_s}{2\pi} = \frac{1}{2\pi\sqrt{L'_{RH}C'_{LH}}} \tag{2.29}$$

$$f_p = \frac{\omega_p}{2\pi} = \frac{1}{2\pi\sqrt{L'_{LH}C'_{RH}}}. \tag{2.30}$$

2.2.1 Balanced and Unbalanced Conditions

Balanced Case

The CRLH-TL can be designed to have no band gap and therefore is said to be balanced when the following conditions are met

$$f_p \stackrel{!}{=} f_s \Rightarrow L'_{RH}C'_{LH} = L'_{LH}C'_{RH} \tag{2.31}$$

or equivalent

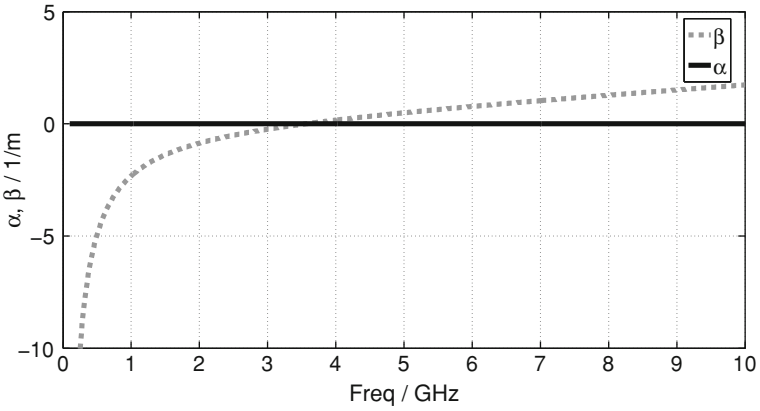

Fig. 2.3 Propagation constant of an exemplary ideal balanced CRLH line ($C_{LH} = 2\,\text{pF}$, $L_{RH} = 1\,\text{nH}$, $C_{RH} = 1\,\text{pF}$, $L_{LH} = 2\,\text{nH}$)

$$Z_c \stackrel{!}{=} Z_{LH} \stackrel{!}{=} Z_{RH}. \tag{2.32}$$

The propagation constant of a balanced CRLH-TL is plotted in Fig. 2.3. The unit cell is made of the following elements: $C_{LH} = 2\,\text{pF}$, $L_{RH} = 1\,\text{nH}$, $C_{RH} = 1\,\text{pF}$, $L_{LH} = 2\,\text{nH}$. Since the series and parallel resonance frequencies are equal, the pole and the zero that were present at f_s and f_p respectively, which have delimited the stop band, cancel each other. As a result, the stop band disappears and a continuous transmission is possible. The zero transition of the phase constant occurs at the transition frequency

$$\omega_0 = \omega_s = \omega_p = \frac{1}{\sqrt{L'_{RH}C'_{LH}}} = \frac{1}{\sqrt{L'_{LH}C'_{RH}}}. \tag{2.33}$$

In regard to the line impedance, it becomes purely real and constant with no dispersive behavior as depicted in Fig. 2.4, resulting in a good matching over a broad frequency spectrum. It can be represented by

$$Z_L = \sqrt{\frac{L'_{RH}}{C'_{RH}}} = \sqrt{\frac{L'_{LH}}{C'_{LH}}}. \tag{2.34}$$

Unbalanced Case

The CRLH-TL is said to be unbalanced when the following condition is met

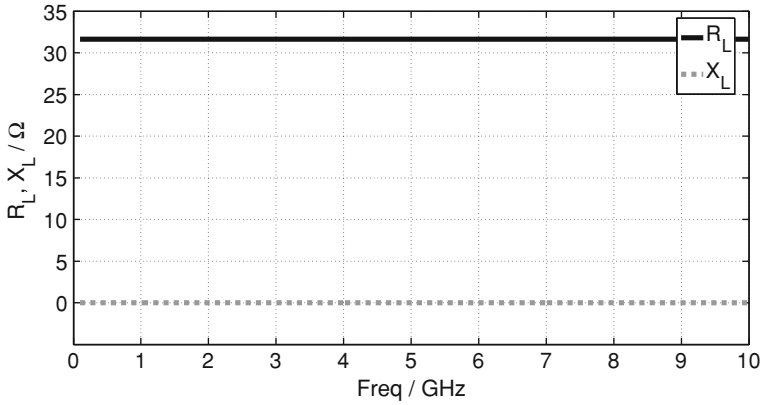

Fig. 2.4 Line impedance of an exemplary ideal balanced CRLH line ($C_{LH} = 2\,\text{pF}$, $L_{RH} = 1\,\text{nH}$, $C_{RH} = 1\,\text{pF}$, $L_{LH} = 2\,\text{nH}$)

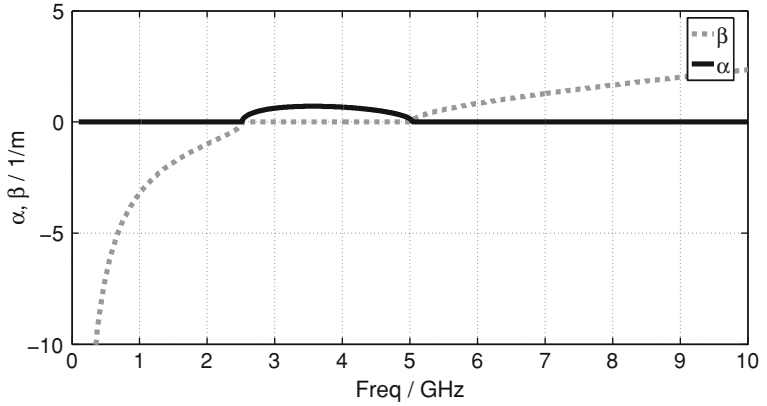

Fig. 2.5 Propagation constant of an exemplary ideal unbalanced CRLH line ($C_{LH} = 1\,\text{pF}$, $L_{RH} = 2\,\text{nH}$, $C_{RH} = 2\,\text{pF}$, $L_{LH} = 1\,\text{nH}$)

$$f_p \neq f_s. \tag{2.35}$$

The propagation constant of an unbalanced CRLH-TL is plotted in Fig. 2.5 and the line impedance can be observed in Fig. 2.6. The unit cell is made of the following elements: $C_{LH} = 1\,\text{pF}$, $L_{RH} = 2\,\text{nH}$, $C_{RH} = 2\,\text{pF}$, $L_{LH} = 1\,\text{nH}$. As a result a band gap is present between the frequencies f_s and f_p for the homogeneous line. In the band gap, the propagation constant takes real values and outside of the band gap imaginary values. Therefore Z' and Y' at these frequencies will have zero immittances introducing a zero and a pole in the characteristic impedance resulting in a zero group velocity. This means, that although a lossless case is assumed, the stop band or gap is present.

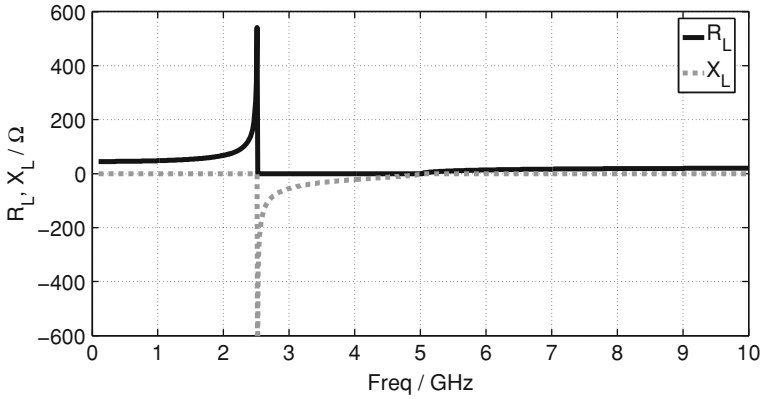

Fig. 2.6 Line impedance of an exemplary ideal unbalanced CRLH line ($C_{LH} = 1\,\text{pF}$, $L_{RH} = 2\,\text{nH}$, $C_{RH} = 2\,\text{pF}$, $L_{LH} = 1\,\text{nH}$)

The line impedance needs a more careful analysis. It has purely imaginary values in the band gap and purely real outside of it. At the frequencies that limit the band gap f_s and f_p, a pole and a zero can exist than can be interchanged by rotating the dimensionless unit cell values. As a result, two CRLH-TL can be constructed with identical resonance frequencies, identical propagation constant and the difference can only be seen in the impedance where it can take positive or negative values inside the band gap. This is important and can be used as an advantage for certain applications where both bands are not needed and a perfect matching can be obtained on the desired band by optimizing the design with the values of the unit cell elements.

2.2.2 Discrete Network Implementation

The ideal CRLH-TL previously described cannot be constructed, a real buildable CRLH-TL can be made by discretizing a homogeneous line in the form of a ladder network circuit by the transition of an infinitesimal unit cell of length dz to a finite unit cell length Δz. In the limit when $\Delta z \to 0$ the CRLH-TL will behave equivalent to the ideal case. To achieve this limit in practice, the size of the unit cell should be smaller than the guided wavelength $\Delta z < \lambda_g/4$ to obtain an electrical length smaller than $\pi/2$. The discretized values of the inductors and capacitors look as follow

$$C_{LH} = C'_{LH}/\Delta z \tag{2.36}$$
$$L_{RH} = L'_{RH} \cdot \Delta z \tag{2.37}$$
$$C_{RH} = C'_{RH} \cdot \Delta z \tag{2.38}$$
$$L_{LH} = L'_{LH}/\Delta z. \tag{2.39}$$

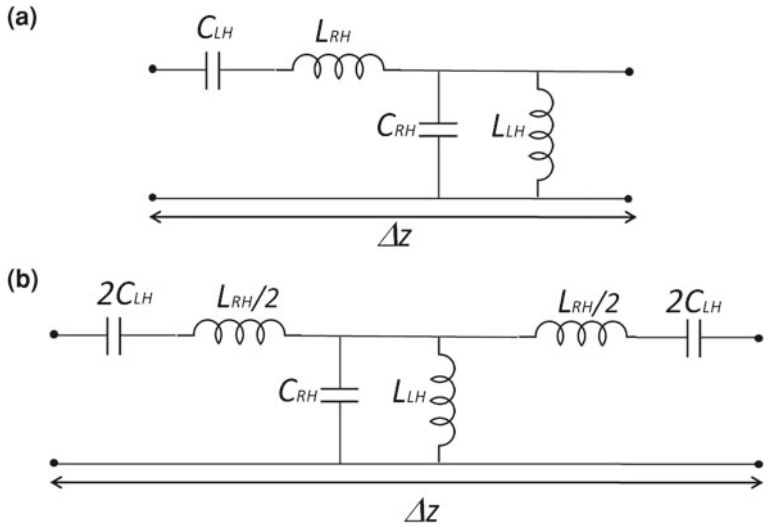

Fig. 2.7 Discrete CRLH unit cell: **a** Asymmetric and **b** Symmetric

Since the transmission line is not infinitely long, it has to be taken into account how the line is terminated. In Fig. 2.7 is shown the case when the CRLH unit cell is terminated in an asymmetric or symmetric way.

For simplicity, the symmetric unit cell will be analyzed and similar analysis can also be conducted for the asymmetric unit cell. The propagation characteristics, namely propagation constant and Bloch impedance, looks as follows [8]

$$\begin{aligned}\gamma &= \pm\frac{1}{\Delta z}\cosh^{-1}\left(1+\frac{ZY}{2}\right)\\ &= \pm\frac{1}{\Delta z}\cosh^{-1}\left(1-\frac{\omega^2}{2}\left(L_{RH}-\frac{1}{\omega^2 C_{LH}}\right)\left(C_{RH}-\frac{1}{\omega^2 L_{LH}}\right)\right)\end{aligned} \tag{2.40}$$

$$\begin{aligned}Z_B &= \pm Z\sqrt{\frac{1}{ZY}+\frac{1}{4}}\\ &= \pm j\omega^2\left(L_{RH}-\frac{1}{\omega^2 C_{LH}}\right)\sqrt{\frac{1}{4}-\frac{1}{\omega^2\left(L_{RH}-\frac{1}{\omega^2 C_{LH}}\right)\left(C_{RH}-\frac{1}{\omega^2 L_{LH}}\right)}}.\end{aligned} \tag{2.41}$$

It should be noted that for both symmetric and asymmetric unit cells the propagation constant is identical and the difference can be seen only in the Bloch impedance. The Bloch impedance represents the characteristic impedance of the discrete implementation of the LC network and takes into account the case where $\Delta z > 0$. In Figs. 2.8

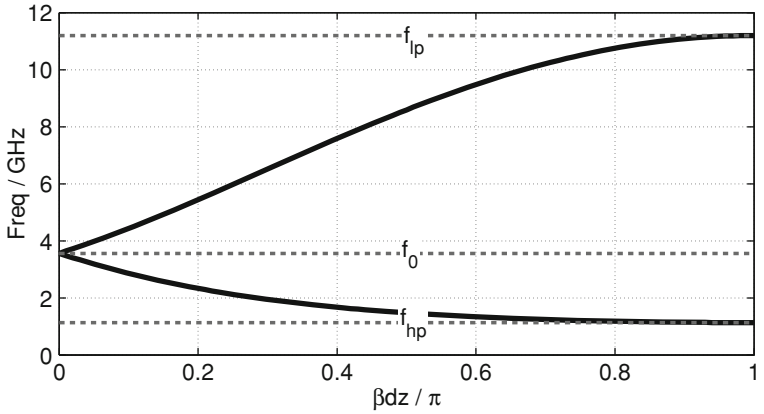

Fig. 2.8 Dispersion diagram for the discrete balanced symmetric CRLH-TL

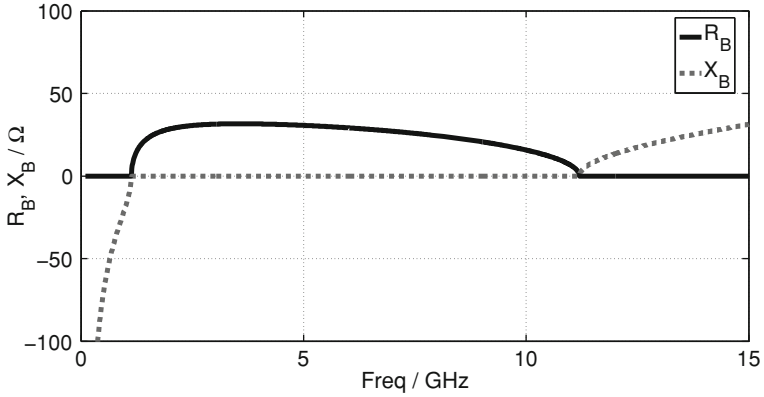

Fig. 2.9 Bloch impedance for the discrete balanced symmetric CRLH-TL

and 2.9 is shown the dispersion diagram and Bloch impedance for the balanced case with lumped elements $C_{LH} = 2\,\text{pF}$, $L_{RH} = 1\,\text{nH}$, $C_{RH} = 1\,\text{pF}$, $L_{LH} = 2\,\text{nH}$. The transition frequency can be calculated with

$$\omega_0 = 2\pi f_0 = \frac{1}{\sqrt[4]{L_{RH}C_{LH}L_{LH}C_{RH}}}. \tag{2.42}$$

The dispersion diagram of a discretized balanced CRLH-TL presented in Fig. 2.8 shows a big difference to the ideal CRLH-TL that can be immediately recognized. The LH and RH bands do not extend to infinity but experience a cutoff frequency f_{hp} at lower frequencies and f_{lp} at higher frequencies. Outside of these boundaries the discrete line will lose the properties of the homogeneous line since the discretization fails. These cutoff frequencies can be obtained by inspection of the input impedance and are given as follows [8]

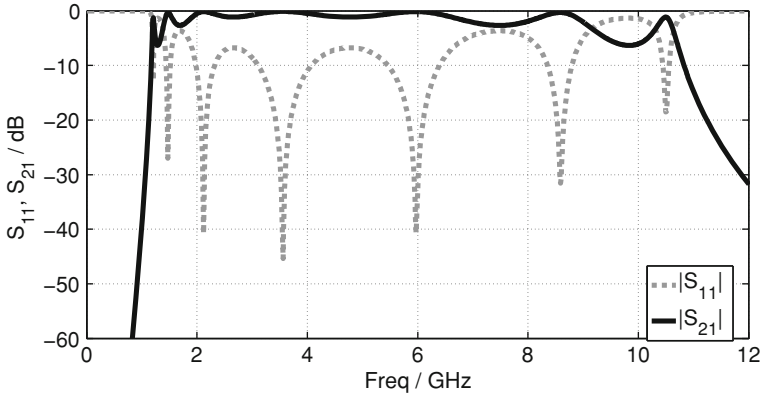

Fig. 2.10 S-parameters for a discrete balanced symmetric CRLH-TL with four identical unit cells ($C_{LH} = 2\,\text{pF}$, $L_{RH} = 1\,\text{nH}$, $C_{RH} = 1\,\text{pF}$, $L_{LH} = 2\,\text{nH}$)

$$f_{hp} = \frac{1}{2\pi}\sqrt{p/2 - \sqrt{p^2/4 - q}} \tag{2.43}$$

$$f_{lp} = \frac{1}{2\pi}\sqrt{p/2 + \sqrt{p^2/4 - q}} \tag{2.44}$$

with

$$p = \frac{1}{C_{RH}L_{LH}} + \frac{1}{L_{RH}C_{LH}} + \frac{4}{L_{RH}C_{RH}} \tag{2.45}$$

$$q = \frac{1}{L_{RH}C_{LH}L_{LH}C_{RH}}. \tag{2.46}$$

The cutoff frequencies effect can also be observed in the Bloch impedance where the impedance is no longer real and constant as with the homogeneous balanced case but becomes purely imaginary outside of the boundaries of the cutoff frequencies.

Finally, in Fig. 2.10 the input reflection S_{11} and forward transmission S_{21} of a discrete symmetric and balanced CRLH-TL are shown. It has four identical unit cells. From the figure can be seen once more the cutoff frequencies f_{lp} and f_{hp} that delimit the transmission band. The influence of the Bloch impedance can also be appreciated in the input reflection S_{11}, the dips represent the points where the terminating port is matched to the input port. Theoretically there should be four peaks on the left handed band, four on the right handed band and one on the transition frequency since we have a balanced structure. In the figure only three peaks can be observed on each band. The missing dips correspond to the cutoff frequencies, at these values the Bloch impedance becomes zero and therefore the input impedance is not equal to the port impedance but takes a zero value. If the structure was unbalanced the dip at the transition frequency would disappear and a band gap would be there instead.

The metamaterial transmission lines will be used in different sensing applications that will be presented in the following chapters. The reason for using them is the possibility of constructing compact sensors that can operate at lower frequencies than with conventional lines. On the other hand, their periodicity can be combined with extraction methods to create a simultaneous monitoring of several samples of material under test (MUT). Finally, even though any capacitance can be used as the sensing element, the most straightforward is the C_{LH} due to its location in the serial branch, especially for planar applications which is the main focus of this work. Additionally, under certain design conditions the C_{LH} can perform with a higher sensitivity than the C_{RH} as will be seen in a comprehensive analysis between them, specifically for sensing applications, in Sect. 4.2.

2.3 Resonant Metamaterial Structures

Additionally to the metamaterial structures using the transmission line approach, there is another type of metamaterial structures based on sub-wavelength resonators, mainly using split ring resonator (SRR). The original topology was first proposed by Pendry [2]. Several different approaches of resonant particles based on SRR have been developed and applied for a number of microwave applications. Their advantages lie on the fact that they are very compact structures with high flexibility in the design process making them suitable for miniaturization purposes. They can be coupled in many different ways by combining them with coplanar, stripline and microstrip designs adding the planarity feature. Depending on the type of resonator and coupling used, different propagation characteristics can be tailored to the desired requirements. It should be emphasized that this approach is named resonant approach because resonators are used as loading elements. The transmission characteristics are qualitatively similar to the CRHL-TL approach presented in the previous section, that means, the resonant approach also exhibits CRLH behavior and can be designed to be balanced and have no stop band. The difference between the two approaches can be visualized on their equivalent circuit models.

2.3.1 Split Ring Resonator

A simple edge coupled SRR is formed by two concentric open metallic rings as depicted in Fig. 2.11. They can have a circular or a square shape. The SRR can be excited by an axial time-varying external magnetic field, which induces current between them. For example, by placing them in the proximity of a microstrip line, the magnetic field present in the line will couple to the SRR. The current loop is closed by the distributed capacitance that appears between the outer and inner ring and the gaps of both of them. They can be modeled as a resonant tank as shown in Fig. 2.11c [9].

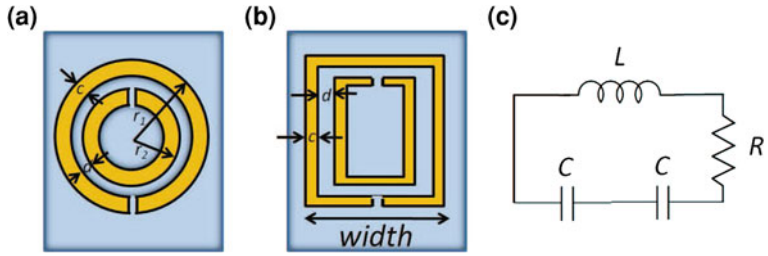

Fig. 2.11 SRR and its most important dimensions: **a** circular design, **b** square design and **c** equivalent circuit

The equivalent circuit has a self-inductance L and a capacitance C associated with each half of the SRR represented as follows

$$C = \pi r C_{pul}, \tag{2.47}$$

where r is the mean radius of the SRR ($r = r_1 - c - d/2$) and C_{pul} is the per-unit length capacitance along the slot between the rings. The total capacitance is the sum of both SRR halves, that is $C/2$. Neglecting losses the total current I is represented as [9]

$$\left(\frac{2}{j\omega C} + j\omega L\right) I = \Sigma \tag{2.48}$$

where Σ is the external excitation. The Eq. 2.48 is valid as long as the perimeter of the ring is smaller than half-wavelength and the capacitance at the gaps neglected so the currents at this place are vanished, therefore, the currents on each ring are assumed to be linear. The voltage across the slots is also constant and the resonant frequency ω_0 can be calculated by solving Eq. 2.48 for $\Sigma = 0$ as follows [9]

$$\omega_0^2 = \frac{2}{LC} = \frac{2}{\pi r C_{pul} L}. \tag{2.49}$$

The main goal of this work is to use an array of SRRs as will be discussed in Sect. 6.2. The SRRs have to be decoupled and detuned from each other in order to have different resonant frequencies and behave independently from each other. From Eq. 2.49 can be deducted that this can be done by changing the size of the SRRs. By changing for example the radius of the SRR the frequency shifts. To simplify the process, it was decided to change only one parameter and the selected one was the radius or width of the SRR particle depending if the are circular or square. In Fig. 2.12 it is shown how the resonant frequency of a particular square ring is affected by changing the width from 0.3 to 4 mm. This proofs that an array of independent SRRs can be done by changing their geometry. This will be very useful in the intended application of this work.

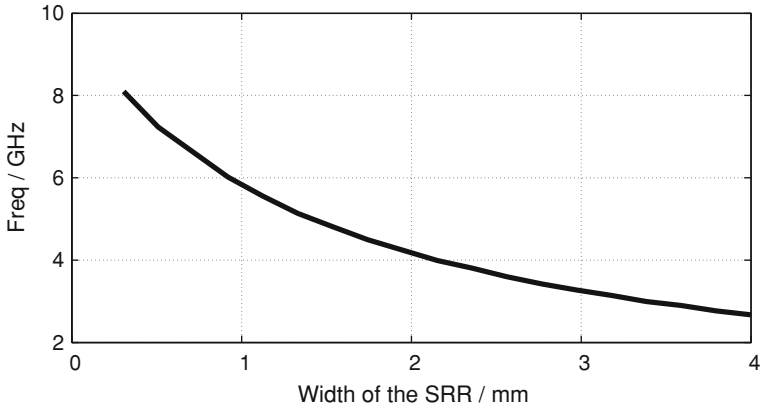

Fig. 2.12 Dependance of SRR resonance frequency f_0 on the width of the SRR

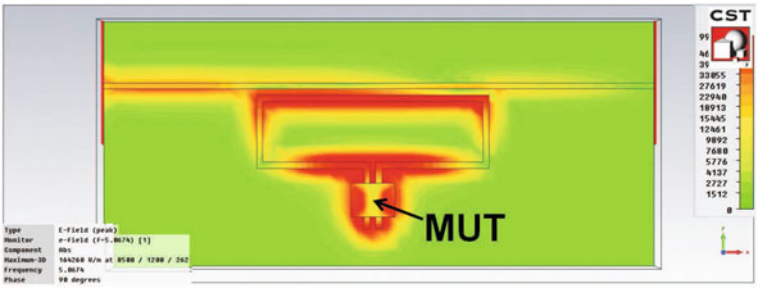

Fig. 2.13 Field distribution on one microstrip excited SRR loaded with a material under test (MUT). The field is clearly stronger around the gap of the ring where the MUT is located and around the coupling to the feeding microstrip line

As it was mentioned in the introduction, another goal of the array of SRRs is to perform dielectric analysis and thermal ablation treatment of organic tissue. For this purpose it is important to analyze the field distribution in order to see if the energy can be focused around the outer gap of the SRR. In Fig. 2.13 an example of a microstrip excited SRR that is in contact with a MUT of $\varepsilon_r = 10$ is depicted. The field distribution is shown and it concentrates around the SRR particle, especially around the MUT where the field has a strength 10 times higher than in the rest of the structure. This ensures an appropriate interaction that will provide the necessary information for making an adequate extraction of the dielectric image of the MUT. Furthermore it ensures a good coupling of the energy into the tissue to be able to perform thermal ablation treatment on the material as will be seen in Chap. 6.

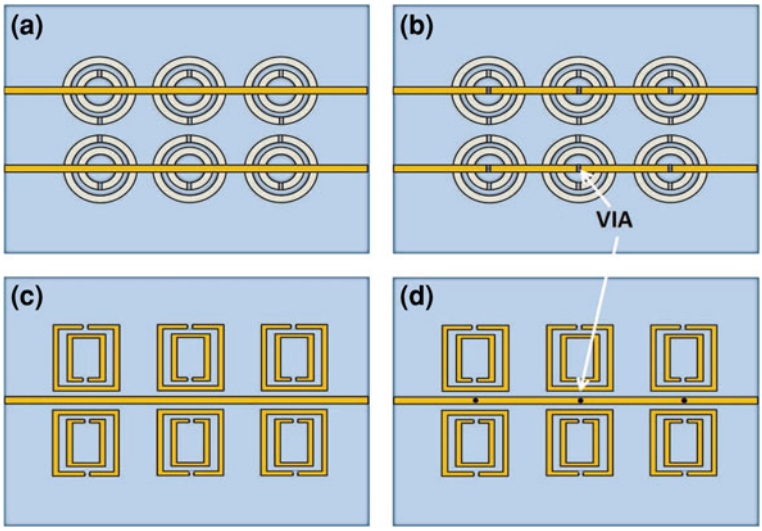

Fig. 2.14 Coplanar waveguide and microstrip technology loaded with SRRs: **a** Coplanar design with negative μ, **b** Coplanar design with negative μ and ε, **c** Microstrip design with negative μ and **d** Microstrip design with negative μ and ε [9]

2.3.2 Transmission Lines Loaded with SRRs

When a periodic array of SRRs is considered, it is possible to obtain either signal propagation or inhibition in a narrow band near the resonance frequency of the SRRs. They behave as lumped resonators and can be designed to have a size much smaller than the wavelength. Due to the resonance present in the SRR medium, it will have extreme permeability both positive and negative around the resonance frequency and therefore no propagation occurs at this frequency. Additionally by including metallic posts or gaps, a simultaneous negative permittivity can also be achieved, i.e. a LHM can be fabricated in a narrow band above the SRR resonance frequency [9].

In Fig. 2.14 four different geometries to excite SRRs are depicted. The first scenario is shown in Fig. 2.14a where a coplanar waveguide is used to excite the SRRs. When a coplanar waveguide is used for this purpose, the SRRs can be etched on the upper or lower side of the substrate for a uniplanar or bi-metal implementation, respectively. The bi-metal choice is preferred since it requires less space to accommodate the SRR and it also reduces the influence on the impedance matching with the line allowing for a better coupling between them. Therefore the bi-metal implementation has a higher coupling and low insertion losses in the desired frequency band [9]. In Fig. 2.14a it is also seen that the SRRs have a slightly different color to represent that they are etched on the back side of the substrate. The resonant frequency can be calculated with Eq. 2.49 and for this specific example with port impedance of 50 Ω a stopband occurs above and below f_0 as seen in Fig. 2.15a. The reason for the

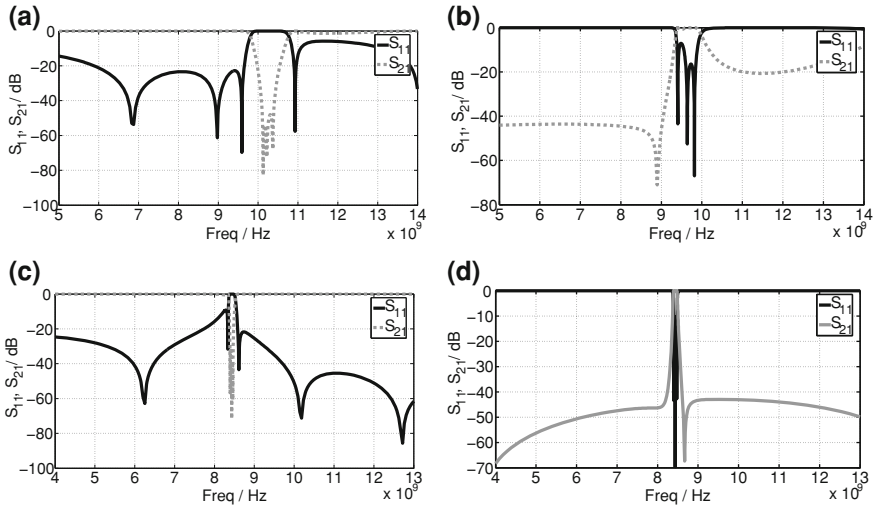

Fig. 2.15 S-parameters of the coplanar waveguide (conductor width = 2.5 mm, gap width = 0.35 mm, r_1 = 0.8 mm, r_2 = 0.4 mm and c = 0.2 mm) and microstrip line (conductor width = 0.2 mm, distance between conductor and rings = 0.2 mm, distance between adjacent rings 1 mm, width of each ring = 2 mm, c = 0.2 mm and d = 0.2 mm) loaded with SRRs: **a** Coplanar design with negative μ, **b** Coplanar design with negative μ and ε, **c** Microstrip design with negative μ and **d** Microstrip design with negative μ and ε (Substrate ε_r = 10.6 and thickness = 254 μm)

stopband is that above f_0 a negative magnetic permeability is present and below a positive permeability in a narrow band also exists resulting in a strong mismatch at the input port of the line. Outside of this frequency range the signal can propagate without any problem, it simply is not affected by the SRRs.

The second possibility corresponds to the first LH-TL implemented using SRR and was reported in [10]. It is a coplanar waveguide with backside etched SRRs and a signal to ground metallic connections (vias) periodically located above the SRRs as shown in Fig. 2.14b. It has simultaneously negative permeability (produced by the SRRs) and permittivity (produced by the vias) in a certain band due to the strips that behave as shunt inductors up to a certain frequency called the plasma or cutoff frequency f_c. As long as f_c is above f_0 a narrow band region will exist where an LH-TL operates above f_0. In this band, signal propagation exists but with backward waves, that is, with negative phase velocity. The propagation is exactly opposite to the data presented in Fig. 2.15a, where the stopband was located, a pass band now takes its place only slightly shifted since it starts exactly above f_0 as seen in Fig. 2.15b. The signal does not propagate outside this band.

The third scenario is done with a microstrip technology design as shown in Fig. 2.14c. The only choice in this particulary case is to etch the SRRs close to the microstrip line to obtain a high magnetic coupling supported by the square shaped SRRs, since the coupling area is larger compared to the circular rings. The propagation is exactly the same as described for the coplanar design of Fig. 2.14a. A

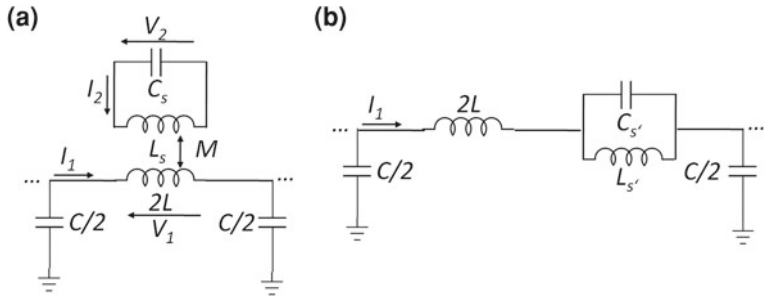

Fig. 2.16 **a** Equivalent circuit for a microstrip loaded with SRRs with negative permeability and **b** circuit model after transformation of the series branch [9]

stopband occurs near f_0 and a good transmission exist outside this band as seen in Fig. 2.15c. The last design is shown in Fig. 2.14d and it includes the microstrip line with square SRR and via holes are included to emulate again shunt inductors and obtain an LH-TL. The behavior is exactly the same as from the structure of Fig. 2.14b. The S-parameters for this case are presented in Fig. 2.15d. Through this work the design of Fig. 2.14c was mainly used so an additional analysis of this scenario will be given.

2.3.3 Microstrip Line Coupled with SRRs as Sensor Elements

The main target of transmission lines based on SRRs in this work is for biomedical applications where the monitoring of dielectric properties of cells or organic tissues is necessary. Furthermore they are used also as a treatment option for cancer tissue when the SRRs are able to heat the tissue and perform thermal ablation. It is not necessary in this case to have them behave as LHM but only as resonators. For this reason the design presented in Fig. 2.14c was selected but it should be emphasized that any of the designs presented in Fig. 2.14 are suitable for this application with its correspondent advantages and disadvantages. The equivalent circuit of the mentioned structure is given in Fig. 2.16a. The model includes a resonant tank to represent the SRR, the host transmission line and the magnetic coupling M between them. Although SRRs can be excited by both magnetic and electric fields, the magnetic coupling is the predominant mechanism and will be considered in the analysis. Since the design under consideration includes microstrip technology, the magnetic coupling cannot be easily calculated by a closed formula and is considered a fitting parameter [9].

The equations for the series and parallel impedance of the Fig. 2.16a are [11, 12]:

$$Z_{SRR}(\omega) = \frac{j\omega(-L + LC_sL_s\omega^2 - 2M^2C_s\omega^2)}{C_sL_s\omega^2 - 1} \tag{2.50}$$

$$Y_{SRR}(\omega) = \frac{2}{j\omega C}, \tag{2.51}$$

and for the transformed model presented in Fig. 2.16b, the equations look as follows [11, 12]:

$$\tilde{Z}_{SRR}(\omega) = \frac{j\omega(L' - L'\omega^2C'_sL'_s + L'_s)}{1 - \omega^2C'_sL'_s} \tag{2.52}$$

$$\tilde{Y}_{SRR}(\omega) = \frac{2}{j\omega C} \tag{2.53}$$

with the following conditions

$$\tilde{L_s} = 2M^2C_s\omega_0^2 \tag{2.54}$$

$$\tilde{C_s} = \frac{L_s}{2M^2\omega_0^2} \tag{2.55}$$

$$\tilde{L} = L - \tilde{L_s}. \tag{2.56}$$

The Bloch impedance for both the original model and the transformed model looks as follows:

$$Z_B = 2\sqrt{\frac{-L + LC_sL_s\omega^2 - 2M^2C_s\omega^2}{C(-4 + 4C_sL_s\omega^2 + \omega^2CL - \omega^4CLC_sL_s + 2\omega^4CM^2C_s)}} \tag{2.57}$$

$$\tilde{Z_B} = 2\sqrt{\frac{-\tilde{L} + \tilde{L}\tilde{C_s}\tilde{L_s}\omega^2 - \tilde{L_s}}{C(-4 + 4\tilde{C_s}\tilde{L_s}\omega^2 + \omega^2C\tilde{L} - \omega^4C\tilde{L}\tilde{C_s}\tilde{L_s} + \omega^2C\tilde{L_s})}}. \tag{2.58}$$

The important frequencies to calculate in order to see if propagation takes place or not are the frequencies where $Z_s = \infty$ (ω_s) and $Z_s = 0$ (ω_0). For the model in Fig. 2.16a are:

$$Z_{SRR} = \infty \tag{2.59}$$

$$L_sC_s\omega^2 - 1 = 0 \tag{2.60}$$

$$\omega_s = \sqrt{\frac{1}{L_sC_s}} \tag{2.61}$$

$$Z_{SRR} = 0 \tag{2.62}$$

$$-L + LC_sL_s\omega^2 - 2m^2C_s\omega^2 = 0 \tag{2.63}$$

$$\omega_0 = \sqrt{\frac{L}{C_s(L_s L + 2M^2)}}. \tag{2.64}$$

And for the model in Fig. 2.16b are:

$$\tilde{Z_{SRR}} = \infty \tag{2.65}$$

$$1 - \tilde{L_s}\tilde{C_s}\omega^2 = 0 \tag{2.66}$$

$$\tilde{\omega_s} = \sqrt{\frac{1}{\tilde{L_s}\tilde{C_s}}} \tag{2.67}$$

$$\tilde{Z_{SRR}} = 0 \tag{2.68}$$

$$\tilde{L} - \tilde{L}\tilde{C_s}\tilde{L_s}\omega^2 + \tilde{L_s}\omega^2 = 0 \tag{2.69}$$

$$\tilde{\omega_0} = \sqrt{\frac{\tilde{L}}{\tilde{L_s}(\tilde{L}\tilde{C_s} - 1)}}. \tag{2.70}$$

Since this is the design that is mainly used in the applications presented in this work and for continuity to the way the analysis was made in the transmission line approach, the propagation characteristics of this model as well as the impedance behavior will be analyzed. The dispersion constant is given by [9]

$$\cos(\beta l) = 1 + \frac{Z_{SRR}(\omega)}{Y_{SRR}(\omega)} \tag{2.71}$$

where $Z_{SRR}(\omega)$ and $Y_{SRR}(\omega)$ are the series impedance and shunt admitance of the circuit model. By applying Eq. 2.71 to the specific equivalent circuit presented in Fig. 2.16, it transforms to [9]:

$$\cos(\beta l) = 1 - \frac{LC\omega^2}{2} + \frac{C/\tilde{C_s}}{4\left(1 - \frac{\omega_0^2}{\omega^2}\right)}. \tag{2.72}$$

From Eq. 2.72, it can be seen that the propagation characteristic changes if the capacitance of the SRR C_s' is affected by loading a material on the SRR. This feature will be thoroughly exploited in the biomedical applications presented in this work. To represent graphically the previous equations, the equivalent circuit of a single SRR coupled to a microstrip line was simulated. The values for the model are $C_s = 1\,\text{pF}$, $L_s = 1\,\text{nH}$, $C = 1\,\text{pF}$, $L = 1\,\text{nH}$ and the unit length taken into account for the extraction of the propagation constant is 5 mm. The coupling between the SRR and the host line was changed from $M = 0$ to represent no coupling to $M = 0.2$ for

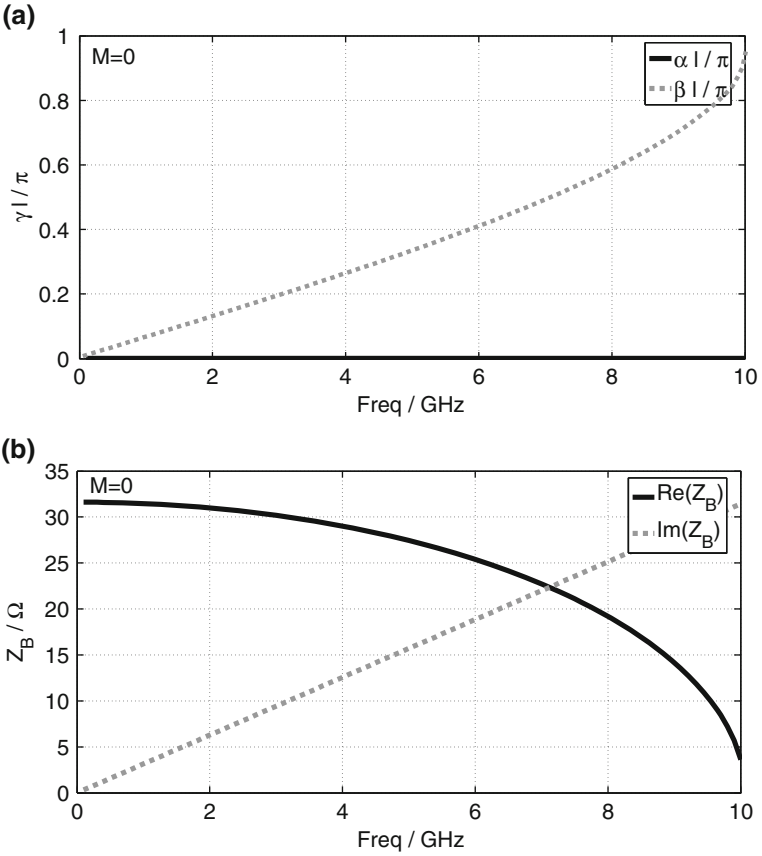

Fig. 2.17 **a** Propagation constant and **b** Bloch impedance of a microstrip line loaded with an SRR ($C_s = 1\,\text{pF}$, $L_s = 1\,\text{nH}$, $C = 1\,\text{pF}$, $L = 1\,\text{nH}$). The coupling between the line and the SRR is $M = 0$

medium coupling and finally to $M = 0.7$ for increased coupling. The results for each of the mentioned cases can be seen in Figs. 2.17, 2.18 and 2.19. Additionally, in these figures the correspondent Bloch impedances are also depicted.

The first scenario with coupling $M = 0$ shows how the host line simple does not see the SRR at all. There is no resonance present and a constant transmission in the frequency band occurs before the discretization starts to fail as for the transmission line approach. The Z_B also shows a semi constant behavior. In the second scenario where the coupling is slightly increased to $M = 0.2$, the host line starts to be influenced by the SRR and a resonance occurs around 5 GHz. In this case the ω_s and ω_0 are almost the same and the expected stop band is very small. This will result in a very sharp peak in the scattering parameters. As the coupling increases to $M = 0.7$, ω_s and ω_0 separate further from each other creating a bigger stop band. This would insert more energy in the structure but the peaks in the scattering parameters would be

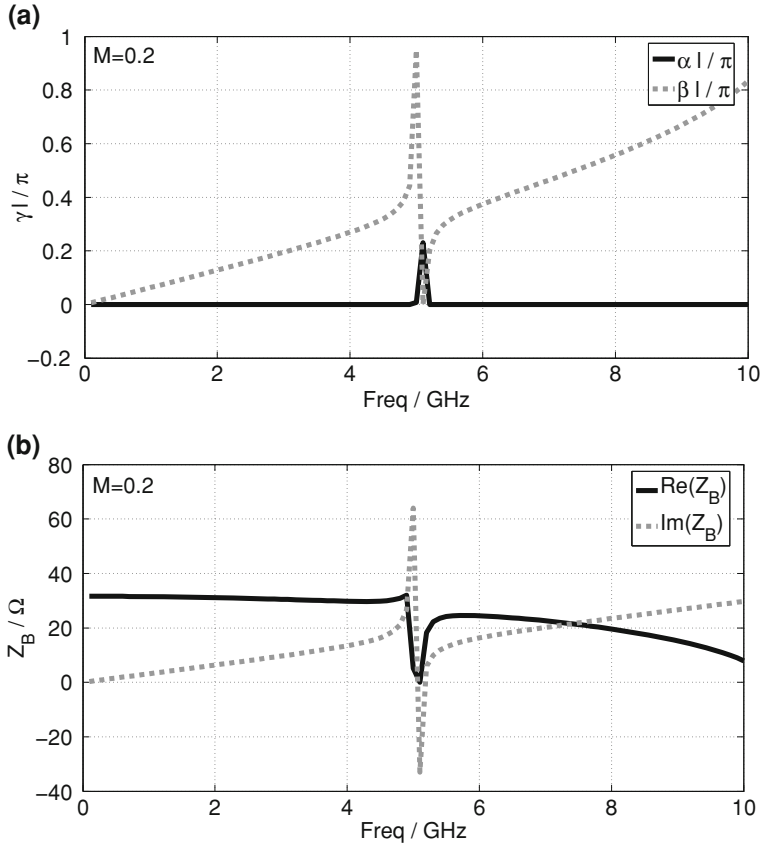

Fig. 2.18 **a** Propagation constant and **b** Bloch impedance of a microstrip line loaded with an SRR ($C_s = 1\,\text{pF}$, $L_s = 1\,\text{nH}$, $C = 1\,\text{pF}$, $L = 1\,\text{nH}$). The coupling between the line and the SRR is $M = 0.2$

wider. For the application presented in this work it is necessary to find a compromise in the coupling since is important to have sharp peaks for using the structure as a sensor but it is also necessary to insert a lot of energy to maximize the efficiency when used for thermal heating of the loading material.

To observe how a small array would behave, the simulated propagation constant and the normalized characteristic impedance for a prototype with two SRRs is shown in Fig. 2.20. A stop band for each SRR is produced in the transmission spectrum due to magnetic resonance for the shown configuration at 0.425 GHz and 1.04 GHz. When the gaps are loaded with a dielectric perturber which increases the overall capacitance, or equivalently the permittivity over the gap, a decrease in the resonance frequency of the loaded SRR will occurred.

Finally, the scattering parameters of an array of four SRRs with slightly different widths to decoupled them is shown in Fig. 2.21. As expected from what has been

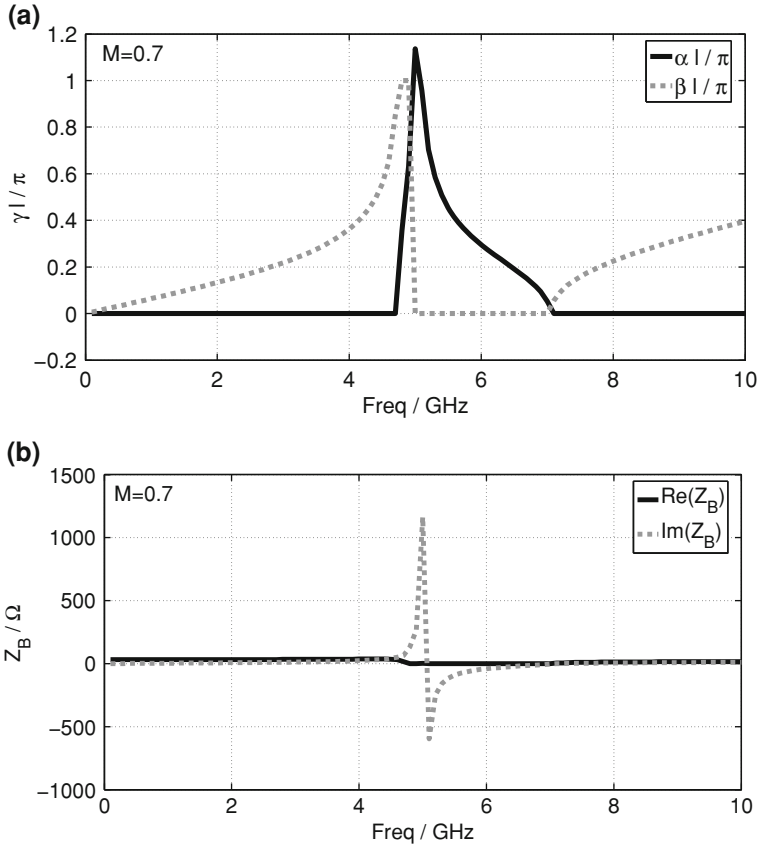

Fig. 2.19 **a** Propagation constant and **b** Bloch impedance of a microstrip line loaded with an SRR ($C_s = 1\,\text{pF}$, $L_s = 1\,\text{nH}$, $C = 1\,\text{pF}$, $L = 1\,\text{nH}$). The coupling between the line and the SRR is $M = 0.7$

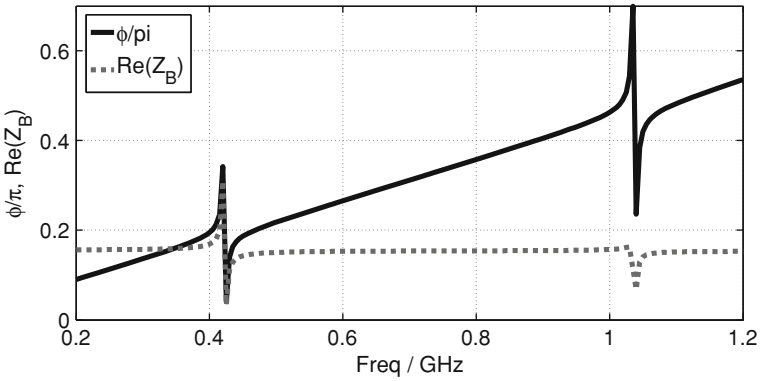

Fig. 2.20 Simulated propagation constant and normalized characteristic impedance of the prototype with two SRRs. Each SRR produces a separate stop band

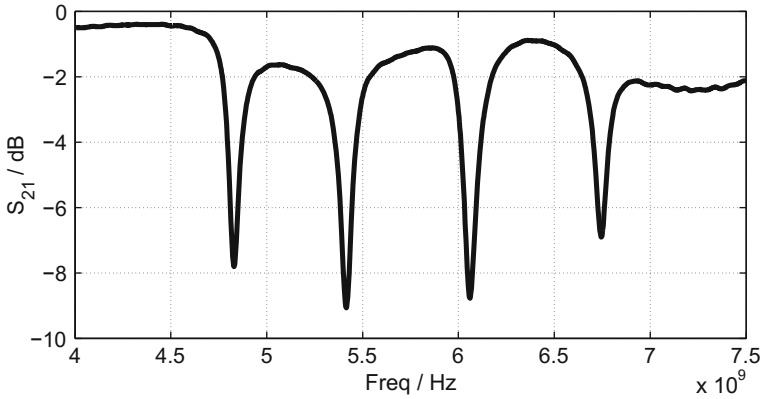

Fig. 2.21 S-parameters of an array of four SRRs. Four independent resonance frequencies can be observed

discussed in this chapter, four resonant peaks can be observed. All SRRs are decoupled and detuned from each other, they are able to interact with a loading material in an independent way and furthermore under a certain scenario they are able to focus the energy in their gaps. The complete discussion has been done without considering any losses coming from the structure itself since they are not necessary for the explanation of the operation principle. They are not an issue in the intended application, the only losses that cause difficulties are coming from the organic material itself as will be discussed in Chaps. 5 and 6.

In summary, metamaterial structures exhibits interesting properties that can be used for sensing applications. Their flexibility in terms of operation frequency, size and geometry can be exploited to create novel, cost-efficient sensor devices. In the following chapters will be studied a novel sensor concept based on this materials and it will be applied in different application scenarios to prove its wide functionality and adaptability.

References

1. C. Caloz, T. Itoh, Application of the transmission line theory of left-handed (LH) materials to the realization of a microstrip LH line, in *Proceedings of the IEEE Antennas and Propagation Society International Symposium*, June 2002. pp. 412–415
2. J. Pendry, A. Holden, D. Robbins, W. Stewart, Magnetism from conductors and enhanced nonlinear phenomena. IEEE Trans. Microw. Theory Tech. **47**(11), 2075–2084 (1999)
3. G. Eleftheriades, A. Iyer, P. Kremer, Planar negative refractive index media using periodically L-C loaded transmission lines. IEEE Trans. Microw. Theory Tech. **50**(12), 2702–2712 (2002)
4. V. Veselago, The electrodynamics of substances with simultaneously negative values of ε and μ. Sov. Phys. Usp. **10**(4), 509–514 (1968)
5. C. Caloz, T. Itoh, *Electromagnetic Metamaterials* (Wiley, Hoboken, 2006)
6. G. Eleftheriades, K. Balmain, *Negative-Refraction Metamaterials* (Wiley, Hoboken, 2005)

7. D. Pozar, *Microwave Engineering* (Wiley, Hoboken, 2005)
8. C. Damm, *Artificial Transmission Line Structures for Tunable Microwave Components and Microwave Sensors* (Shaker Verlag, Aachen, 2011)
9. R. Marques, F. Martin, M. Sorolla, *Metamaterial with Negative Parameters* (Wiley, Hoboken, 2008)
10. F. Martín, F. Falcone, J. Bonache, R. Marqués, M. Sorolla, Split ring resonator based left handed coplanar waveguide. Appl. Phys. Lett. **83**, 4652–4654 (2003)
11. F. Aznar Ballesta, Caracterización de Nuevos Resonadores Metamaterial, Líneas de Transmisión Artificiales y Aplicación en el Diseño de Circuitos de Comunicaciones, Ph.D. dissertation, Universitat Autònoma de Barcelona, Departament d'Enginyeria Electrònica, July 2009
12. F. Aznar Ballesta, Revisión del modelo circuital de una línea de transmisión metamaterial basada en split ring resonators (srrs), Master's thesis, Universitat Autònoma de Barcelona, Departament d'Enginyeria Electrònica, 2009

http://www.springer.com/978-3-319-06040-8

Planar Metamaterial Based Microwave Sensor Arrays for Biomedical Analysis and Treatment

Puentes Vargas, M.

2014, XIV, 153 p. 131 illus., 34 illus. in color., Hardcover
ISBN: 978-3-319-06040-8